Final Draft

of the original manuscript

Vacchi, G.; Silva, R.; Plaine, A.; Suhuddin, U.; Alcantara, N.; Sordi, V.; Rovere, C.:

Refill friction stir spot welded AA5754-H22/Ti-6Al-4V joints: Microstructural characterization and electrochemical corrosion behavior of aluminum surfaces.

In: Materials Today : Communications. Vol. 22 (2020) 100759.

First published online by Elsevier: 08.11.2019

https://dx.doi.org/10.1016/j.mtcomm.2019.100759

Refill friction stir spot welded AA5754-H22/Ti-6Al-4V joints: Microstructural characterization and electrochemical corrosion behavior of aluminum surfaces

G.S. Vacchi[a,*], R. Silva[a], A.H. Plaine[b,c], U.F.H. Suhuddin[c], N.G. Alcântara[a], V.L. Sordi[a], C.A.D. Rovere[a,*]

[a] Munir Rachid Corrosion Laboratory, Materials Engineering Department, UFSCar – Federal University of São Carlos, Rodovia Washington Luis Km 235, 13565-905, São Carlos, SP, Brazil
[b] Mechanical Engineering Department, UDESC – Santa Catarina State University, Paulo Malschitzki Street 200, 89219-710, Joinville, SC, Brazil
[c] Helmholtz-Zentrum Geesthacht, Institute of Materials Research, Materials Mechanics, Solid-State Joining Processes, Max-Planck-Str.1, Geesthacht, Germany

Abstract

The present study assessed the influence of refill friction stir spot welding (RFSSW) process on the microstructure and electrochemical corrosion behavior of the AA5754-H22 alloy surface of an AA5754-H22/Ti-6Al-4 V overlapped joint. The results demonstrate that the RFSSW process promotes substantial microstructural changes along the welded joint, which, in turn, reflect directly on the mechanical properties and corrosion behavior of distinct welding regions. The potentiodynamic polarization tests and electrochemical impedance spectroscopy measurements indicate that the stir zone region has better corrosion resistance than the other RFSS welded regions [heat affected zone and base metal] due to higher homogeneity and microstructure refinement. The achieved results are evidence that the RFSSW process is an interesting alternative for the welding of overlapping dissimilar joints.

1. Introduction

The 5xxx series aluminum-magnesium (Al-Mg) is a strain hardened aluminum alloy which are widely used in the aeronautical industry in sheet form due to their favorable specific strength and corrosion resistance, as well as their relatively low production cost [1]. However, in certain applications, where high mechanical strength and high corrosion resistance are required, Al-Mg alloys are substituted with titanium (Ti) alloys, such as Ti-6Al-4 V, despite their higher cost [2].

In order to combine the low weight and cost of the aluminum (Al) alloy with the high mechanical and corrosion resistance of the Ti alloy, hybrid structures comprised of Ti-Al alloys have recently been developed [2,3]. However, physical and chemical differences between these materials complicate their joining by means of conventional welding technologies. In addition, the metal joining processes currently in use have a high energy cost (resistance welding) and/or increase the weight of the structure (riveting) [4,5]. Due to these challenges associated with existing metal joining processes, the development of new spot welding processes that reduce energy cost and do not increase the weight of the structure are necessary to more efficiently produce multi-material Al-Ti structures. Thus, an emerging alternative is Refill friction stir spot welding (RFSSW), which is a solid-state welding process derived from friction stir welding (FSW) [6–9].

RFSSW was developed in Germany (HZG) in 2005 and can be used in several combinations of dissimilar overlap joints with satisfactory results, e.g., Al-Al, Al-Mg, Al-Steel and Mg-Mg [10]. Moreover, a recent study by our research group [11] has shown that RFSSW promotes significant improvement to corrosion resistance in the stir zone (SZ) region of a precipitation-hardened aluminum alloy (AA6181-T4), making it attractive for spot joining overlapping sheets. Nevertheless, for each new joint combination, RFSSW process requires the optimization of welding parameters to produce defect-free, structurally sound and reliable welds. In addition, the optimization is also necessary due to microstructural changes that occur during joining, which can modify the mechanical properties and corrosion resistance of the welded joint and cause premature component failure [12].

Plaine et al. [13], when evaluating the influence of dwell time and rotational speed on lap shear strength, optimized the RFSS welding parameters for a dissimilar joint between a strain hardened aluminum alloy (AA5754-H22) and a titanium alloy (Ti-6Al-4 V). These authors [10] also reported that the microstructural changes occurred mainly in the Al sheet, however, they did not conduct any additional research with regaation of titanium and aluminum alloys.

Considering the scarcity of research on the corrosion resistance of strain hardened aluminum alloys welded by RFSSW and given that localized corrosion resistance is a key parameter for the use of the researched (and RFSS Welded) alloys in industrial applications, the objective of the current study was to evaluate the electrochemical corrosion behavior on the surface of the AA575-H22 alloy, which was overlap welded with the Ti-6Al-4 V alloy by means of RFSSW. The microstructural changes on the surface of the AA575-H22 alloy sheet were assessed by optical microscopy, scanning electron microscopy with energy dispersive X-ray spectroscopy (SEM/EDS), electron backscatter diffraction (EBSD) and hardness measurements. The localized corrosion resistance was analyzed by potentiodynamic polarization tests and passive film properties were characterized by electrochemical impedance spectroscopy measurements.

2. Experimental procedure

2.1. Materials

The materials used in the present study were 2-mm-thick sheets of AA5754-H22 and Ti-6Al-4 V with dimensions measuring approximately 47.0 mm x 26.0 mm. The AA5754-H22 has a nominal composition (wt. %) of 0.04 Ti, 0.15 Si, 0.20 Fe, 0.05 Cu, 0.08 Mn, 3.10 Mg, Al as the balance and the Ti-6Al-4 V presents the nominal composition (wt.%) of 6.25 Al, 0.14 Fe, 3.91 V, 0.02 C, 0.13 O, Ti as the balance. Both nominal compositions were provided by the manufacturers.

The joints were manufactured at the Helmholtz Zentrum Geesthacht Institute for Materials Research with an overlap configuration by an RPS 200 RFSSW machine using a rotation speed of 2000 rpm/min, a dwell time of 2 s, a sleeve plunge depth of 1.8 mm and a clamping force of 12 kN [14]. The utilized welding tool was comprised of a clamping ring, sleeve and pin, with diameters of 18.0, 9.0 and 6.4 mm, respectively. It should be mentioned that RFSS welding was performed with the aluminum alloy placed over the titanium alloy and the tool sleeve plunge remained on the top sheet to avoid both excessive tool wear and formation of intermetallic compounds. Due to the fact that the Ti-6Al4 V alloy microstructure does not change [15], the

analyses focused on the AA5754-H22 alloy surface. Fig. 1(a–c) presents the AA5754-H22 surface, the welding region zoom and a cross-sectional view of the welded joint.

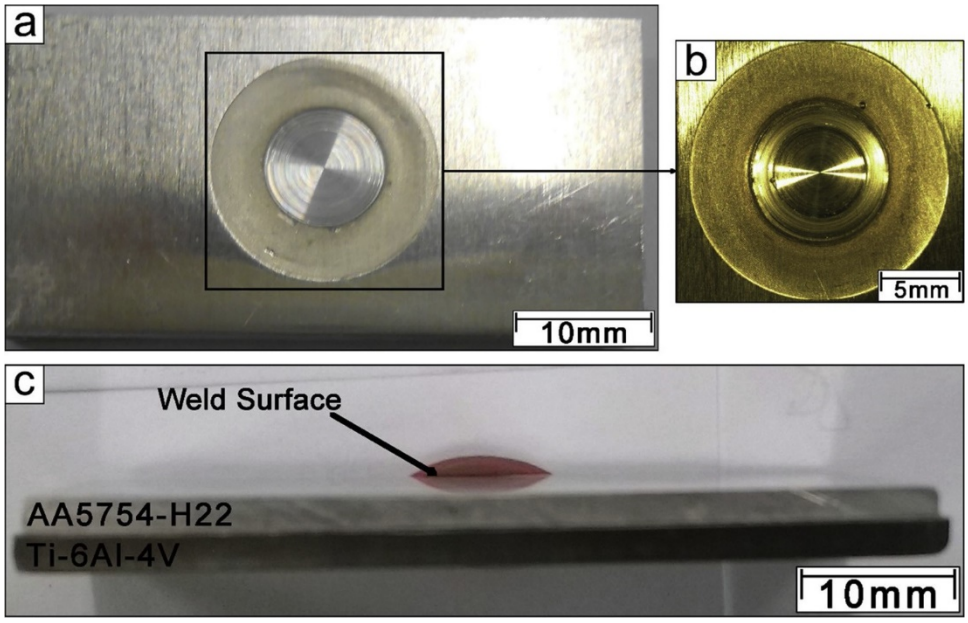

Fig. 1. (a) Surface of the AA5754-H22; (b) Macroscopic image of the refill friction stir spot welded aluminum surface; (c) The cross section of the welded joint.

2.2. Hardness measurements

Vickers microhardness mapping was performed on the surface of an AA5754-H22 alloy to identify the transitions between the different welding regions and to evaluate the microstructural variation in mechanical strength in the welded regions. Fig. 2 details the mapped region. The measurements were carried out using a spacing of 0.5 mm between two adjacent indentations and a dwell time of 10 s, which had a load of 300 g.

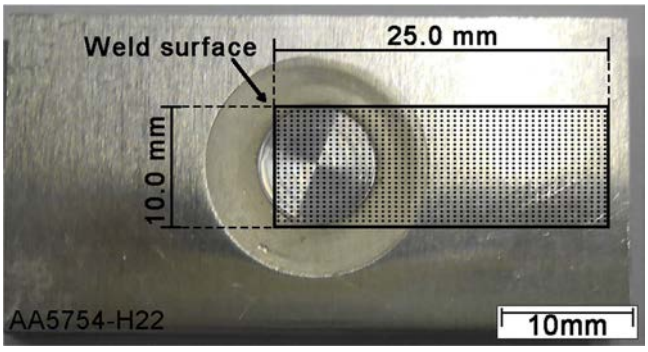

Fig. 2. Vickers microhardness mapping region of the AA5754-H22 welded surface.

2.3. Microstructure characterization

For the microstructural characterization, the surface of the studied material was carefully sanded with SiC abrasive paper up to #1500 grit and polished with 1.0 μm alumina suspension. The sample was subsequently electrolytically attacked with Barker's reagent (5 mL of HBF_4 in 200 mL H_2O), using 20 V for 120 s. The resulting microstructure was examined with an optical microscope using polarized light (OM). After characterizing the different welding regions using an OM, the same sample was repolished with 1.0 μm alumina suspension and analyzed by SEM/EDS and EBSD.

2.4. Electrochemical corrosion tests

All electrochemical tests were performed using a conventional three-electrode cell. A silver/chloride silver (Ag/AgCl in saturated KCl) electrode was used as a reference and a platinum auxiliary electrode was used as a counter. The working electrodes (exposed circular area of 0.215 cm^2), which consisted of samples from different welding regions [i.e., base metal (BM), heat affected zone (HAZ) and stir zone (SZ)], were carefully wet sanded to a #600-grit silicon carbide (SiC) paper finish, then washed with distilled water and air dried before conducting the electrochemical tests. Two naturally aerated solutions at a temperature of 25 °C were used in the electrochemical corrosion tests: (1) a 0.5 M sodium sulfate (Na_2SO_4) solution for impedance analyses and (2) a 0.01 M sodium chloride (NaCl) with an added 0.1 M Na_2SO_4 solution for polarization tests. Na_2SO_4 was added to improve pitting potential (E_{pit}) identification during the aluminum alloy polarization tests [16]. The measurements were performed using a Reference 3000™ Potentiostat/Galvanostat/ZRA from Gamry Instruments.

The potentiodynamic polarization tests started after 30 min of immersion. This immersion procedure was followed for the samples to reach a quasi-stationary value of open circuit potential (E_{oc}) in the 0.01 M NaCl + 0.1 M Na_2SO_4 solution. The potentiodynamic polarization tests were performed at a scan rate of 1 mV/s from an initial potential of 300 mV below E_{oc} until the current density increased to 10 μA/cm^2. The mean values of pitting potential (E_{pit}) were obtained by taking five independent measurements. After the polarization tests, each welding region was analyzed by SEM/EDS in order to identify the morphology of the corrosion attack.

The electrochemical impedance spectroscopy (EIS) measurements started after 60 min of immersion. This amount of time was required to ensure that all samples had reached a steady-state in the 0.5 M Na_2SO_4 solution and the acquired potential value was considered to be the open-circuit potential (E_{oc}). EIS tests were conducted at a frequency ranging from 0.01 Hz to 100 kHz with a 10 mV amplitude signal at E_{OC}. The EIS results were obtained from three independent measurements. The impedance spectra analysis was completed by fitting the experimental results to the equivalent circuits using Echem Analyst™ Software from Gamry Instruments. The goodness-of-fit of the EIS data to the equivalent circuits was judged by using Chi-square value (χ^2), where the χ^2 value represents the sum of the square of the differences between theoretical and experimental points.

3. Results and discussion

Fig. 3 shows the OM macrostructure of the Al surface for the AA5754-H22/Ti-6Al-4 V RFSS welded joint, where the rolling direction of the AA5754-H22 alloy and the regions associated with the clamping ring, sleeve and pin are accurately indicated. The presence of six different regions in the macrostructure is observable, namely (from left to right): BM (a), HAZ (recrystallized) (b), HAZ (grain growth) (c), the thermo-mechanically affected zone (TMAZ) (d), SZ comprising the sleeve (e) and the pin (f) regions. The BM [Fig. 4(a)] displays a deformed structure with the grains oriented vertically, which is a result of the base material hardening treatment -H22 (strain hardened and partly annealed). Fig. 4(b) exhibits the recrystallized HAZ region, note that the previously deformed grains have changed to a fine equiaxial structure. This structural change is a consequence of the thermal cycle imposed by the RFSS welding process, which promotes an increase in temperature within this region and, in turn, causes a static recrystallization. Additionally, in regions closer to the SZ, where the temperatures reached are considerably higher [Fig. 4(c)], the resulting microstructure demonstrates a coarser-grained structure in comparison to the recrystallized region [Fig. 4(b)]. This is due to the availability of a higher amount of energy that initially recrystallizes the grains, and then promotes their growth.

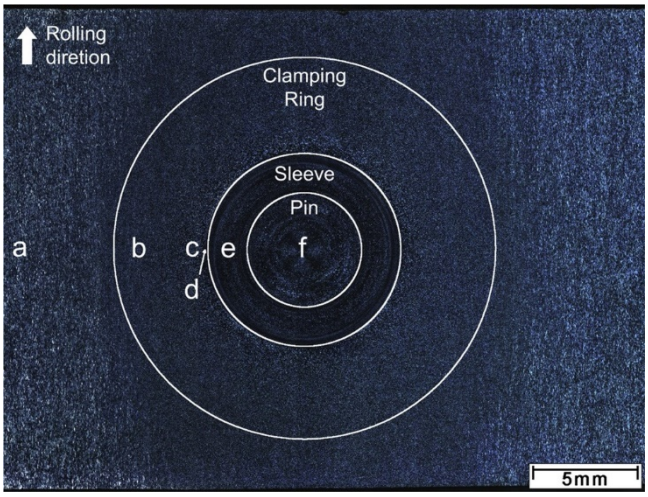

Fig. 3. Macroscopic image of the refill friction stir spot welded surface of the AA5754-H22: (a) BM, (b) HAZ (recrystallized), (c) HAZ (grain growth), (d) TMAZ, SZ comprising (e) the sleeve and (f) the pin regions.

When evaluating an AA5083-H19 alloy welded by FSW, Peel et al. [17], also observed a recrystallized microstructure in the HAZ that was associated with energy generated through the welding process, in addition to internal energy already stored within the deformed base material. Contrarily, when Fonda et al. assessed an AA5456-H116 alloy welded by means of FSW [18], they identified a HAZ with a recovered microstructure formed by equiaxial subgrains with some deformation (i.e., a low dislocation density). The authors cited the thermal cycle imposed by the welding process as the cause. Therefore, the presence of a HAZ with a recovered or recrystallized microstructure in strain hardened aluminum alloys, such as the 5xxx series, depends of two factors: the degree of BM deformation and the thermal cycle imposed by the welding process.

The TMAZ region in Fig. 4(d) displays a recrystallized and slightly elongated microstructure. This is due to the high temperature achieved in this region, in addition to the deformations

promoted by the RFSSW tool, which stretch and line them up in the direction of the sleeve rotation. Diversely, in the SZ – where the sleeve [Fig. 4 (e)] and the pin [Fig. 4(f)] regions are observable in the periphery and center of the welding spot, respectively – an equiaxial microstructure is present. The severe plastic deformation and high temperatures at which SZ was subjected during the RFSSW process resulted in dynamic recrystallization of the deformed aluminum matrix.

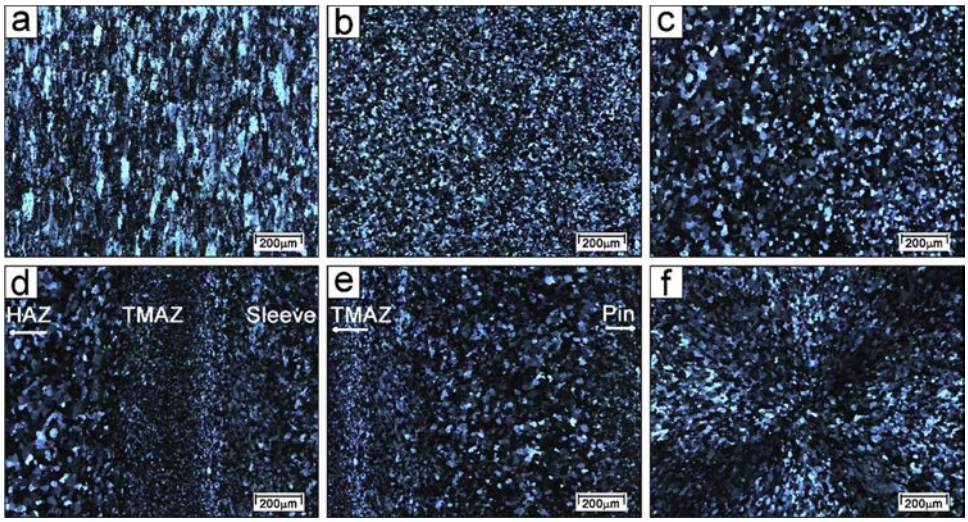

Fig. 4. OM of distinct welding regions: (a) BM; (b) HAZ (recrystalized); (c) HAZ (coarsed grains); (d) TMAZ; (e) Sleeve region; (f) Pin region.

Fig. 5 depicts SEM images from the BM [(a) and (e)], HAZ [(b) and (f)], sleeve region [(c) and (f)] and pin region [(d) and (g)]. The figure demonstrates two different types of precipitates in the BM: (1) a dark color precipitate (in smaller amount) and a lighter color one (in larger amount). Both precipitates are non-uniformly dispersed throughout the BM matrix. EDS composition analyses (Table 1) revealed that the lightcolored precipitates are rich in Fe, Mn, Mg and some contain Si, while the dark-colored precipitates are rich in Si and Mg. Fuller et al. [19] evaluated the effect of friction stir processing on 5083-H321/5356 Al arc welds and used the Transmission electron microscopy (TEM) to identify the presence of similar precipitates to those observed in the present study. It is well known that Fe is a dominant impurity present in most commercial Al alloys. The presence of Fe-rich intermetallic precipitates is related to the low solubility of Fe in Al, which has a maximum solubility of around 0.04 wt.% at 655 °C, decreasing to 0.001 wt. % below 430 °C, in addition to the high thermodynamic stability of Ferich precipitates (melting points higher than 700 °C) [20,21]. On the other hand, the Mg_2Si precipitates, which are less thermally stable than Fe-rich precipitates, are formed through eutectic dissociation in the molten alloys [21].

The HAZ, Fig. 5(b) and (f), also presented the same precipitates and had a similar size as those found in the BM. It is important to mention that in both the BM and HAZ, the precipitates have a non-uniform distribution, which is associated with the alignment of these precipitates with the rolling direction during the hardening process, remaining unchanged even after the static recrystallization of the HAZ. Similar results were observed by Attallath et al. [21] for the AA5251H34 alloy, who noted that the precipitates were oriented in the rolling direction due to

the cold working process of the BM. Conversely, in the sleeve region exhibited in Fig. 5(c) and (g), only the lighter precipitates were present. In addition, they not only presented a smaller size, but were also uniformly distributed along the bulk. This suggests that the Mg_2Si precipitates were dissolved or broken down into sizes smaller than the resolution of the performed SEM analysis [21].

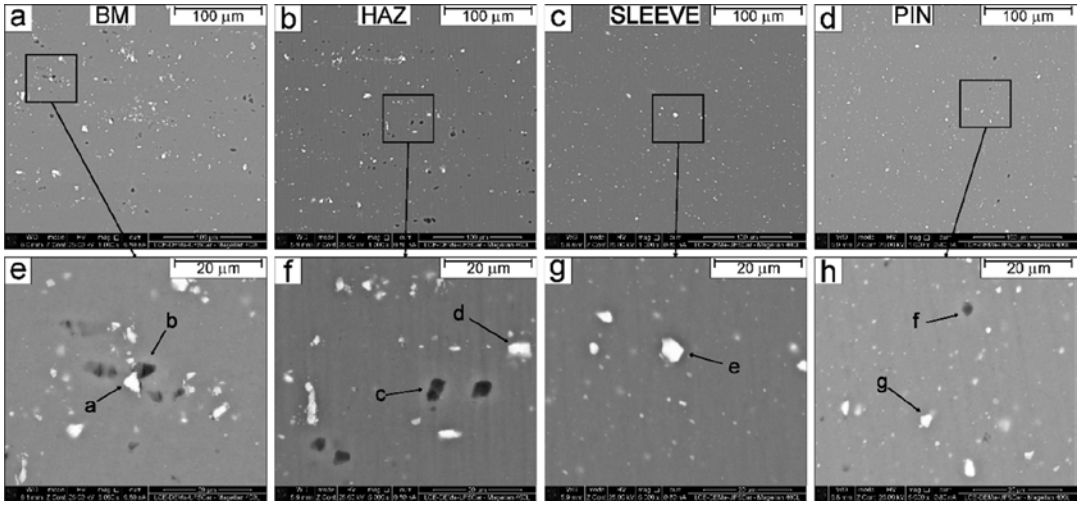

Fig. 5. SEM micrographs of the distinct welding regions: (a) and (e) BM; (b) and (f) HAZ; (c) and (g) Sleeve; (d) and (h) Pin.

In the pin region, Fig. 5(d) and (h), the two types of precipitates are observable again, but more uniformly and in sizes smaller than in the BM and HAZ regions. This difference suggests that the RFSS welding process promoted different strain rates along the SZ, which resulted in a precipitate size difference in each region. McNelley et al. [22] observed similar results when evaluating the mechanisms of recrystallization during friction welding in aluminum alloys. According to their study, the precipitate size decreased as the rate of deformation increased. Furthermore, this correlation may be related to the penetration of the sleeve into the material, resulting in a greater deformation than that of the pin region, which only retracts to compensate for the volume displacement that occurs due to the penetration of the sleeve.

Table 1 EDS composition analyses performed from precipitates present in different welded regions.

Weld Region	Point	Composition (wt%)						Precipitates
		Al	Mg	Si	Fe	Mn	O	
BM	A	81.88	3.75	0.66	12.63	1.09	0.00	Al(Fe,Mg,Mn,Si)
BM	B	71.15	11.88	11.69	0.00	0.00	5.28	Mg_2Si
HAZ	C	66.87	2.99	15.62	0.00	0.00	14.52	Mg_2Si
HAZ	D	82.15	2.85	0.00	13.77	1.23	0.00	Al(Fe,Mg,Mn)
Sleeve	E	82.25	2.87	0.00	13.50	1.38	0.00	Al(Fe,Mg,Mn)
Pin	F	60.14	3.95	19.33	0.00	0.00	16.58	Mg_2Si
Pin	G	78.90	2.57	0.00	17.17	1.36	0.00	Al(Fe,Mg,Mn)

Fig. 6(a) and (b) show the hardness mapping and Fig. 7(a–f) presents the EBSD microstructural evolution of the AA5754-H22 surface welded by RFSSW. It can be noted in Fig. 6(a) and (b) that the BM exhibits a higher hardness value (approximately 85 $HV_{0.3}$) in comparison to the HAZ and the SZ. Contrarily, the lowest hardness values (around 55 $HV_{0.3}$) are observed in the HAZ. Through EBSD images [Fig. 7(d) and (f)], it is apparent that this region is constituted by three different microstructures, one closer to the SZ [(Fig. 7(d)] that presented a coarser grain (~35 μm), a second in the middle of the HAZ [(Fig. 7(e)] with a more refined microstructure (~15 μm) and a third near the BM [Fig. 7(f)] that presented a partially deformed microstructure (~12 μm). As previously discussed, this microstructural variation is due to the thermal cycle imposed by the welding process, which promoted recrystallization and grain growth in the region closer to the SZ, a recrystallization in the middle of the HAZ and recovery in the region closest to the BM.

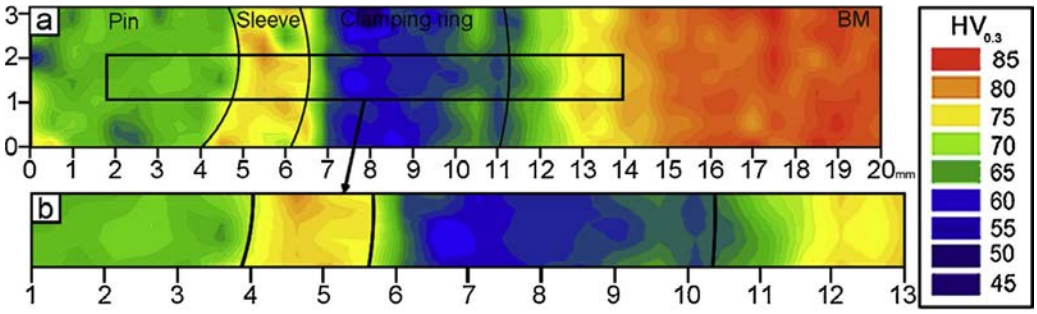

Fig. 6. (a) hardness mapping of the AA5754-H22 FSp welded surface, (b) Hardness mapping of the highlighted region in (a).

Furthermore, intermediate hardness values (between 65 $HV_{0.3}$ and 75 $HV_{0.3}$) are observed in the SZ. It is worth mentioning that this region also presented a microestructural variation, as seen in the HAZ [Fig. 7(b) and (c)], however, the variation in this case is likely caused by the deformation rate, which is demonstrated by the fraction variations of the low angle boundaries (Table 2) [23]. Fig. 7(g) illustrates that the microstructure associated with the pin region has a mean grain size of 30 μm, which is greater than the average grain size of about 10 μm observed in the sleeve region [Fig. 7(h)].

In order to evaluate the corrosion behavior in distinct welding regions, polarization and impedance measurements were performed. It should be pointed out that in these measurements the TMAZ couldn't be analyzed separately because the exposed circular area to the corrosive media had a diameter of 5.23 mm that was higher than the TMAZ region (0.5 mm). Therefore, due to the small size of TMAZ region, only three welding regions were considered in the potentiodynamic polarization tests (BM, HAZ and SZ). Fig. 8(a) shows the potentiodynamic polarization tests for the different welding regions (BM, HAZ, SZ). Note that the three RFSS welding regions display a potential-current behavior typical of passive metals in a chloride environment. Thus, with the increase of electrode potential from 300 mV below E_{oc} to anodic direction, polarization curves passing initially through the cathodic region, then through the E_{corr} and passive region (where the passive current density remains reasonably constant) and, finally, to the localized breakdown region of the passive oxide film (where the current suddenly begins to increase with potential, defining the E_{pit}).

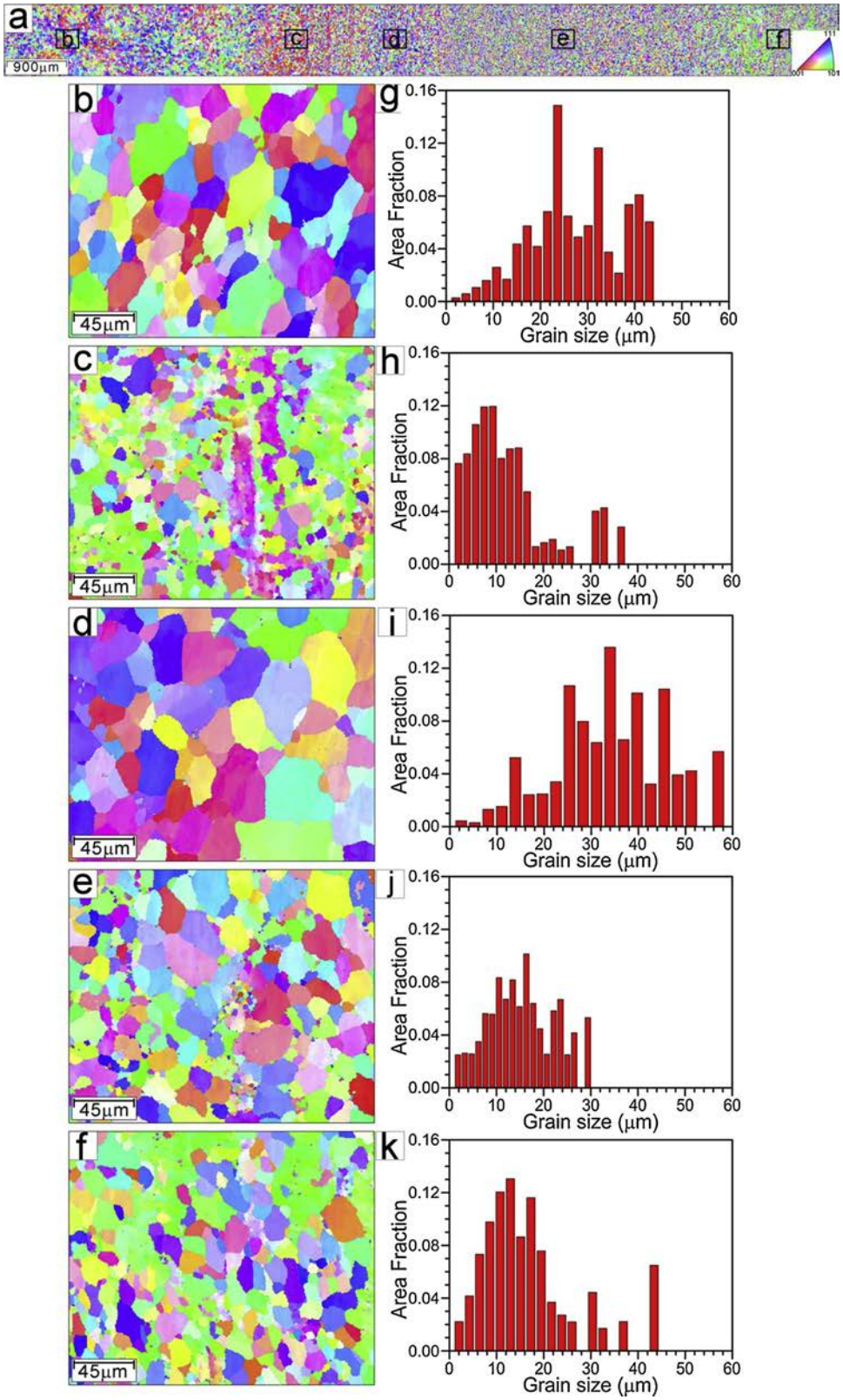

Fig. 7. (a) Grain orientation mapping of the detailed region in Fig. 6(b); Grain orientation mapping of the region: (b) Pin, (c) Sleeve, (d) HAZ (grain growth), (e) HAZ (recrystallized) and (f) BM; Grain size distribution of: (g) Pin region; (h) Sleeve region; (i) HAZ closer to SZ; (j) HAZ distant of SZ; (k) BM.

Table 2 Rotation angle boundaries (fraction) of different welding regions of an AA5754H22 welded surface.

Weld Region	Rotation angle boundaries fraction		
	2° to 5°	5° to 15°	15° to 180°
Pin	0.226	0.114	0.659
Sleeve	0.313	0.173	0.514
HAZ closer to SZ	0.274	0.108	0.618
Middle region from HAZ	0.203	0.036	0.760
HAZ closer to BM	0.337	0.104	0.559

However, the distinct welding regions had a slight variation in the anodic behavior, which is shown in the E_{corr} and E_{pit} mean values presented in Fig. 8(b). Note that E_{corr} mean values of distinct welding regions range from −823 $mV_{Ag/AgCl}$ to −782 $mV_{Ag/AgCl}$. Likewise, E_{pit} mean values range from −378 $mV_{Ag/AgCl}$ to −322 $mV_{Ag/AgCl}$. Nevertheless, it should be mentioned that the relatively high dispersion associated with the potentiodynamic polarization measurements may be related to the relatively small area (0.215 cm^2) of the working electrode (to separate the distinct welding regions) as well as the density and size variation of the precipitates at each new measurement [11,24].

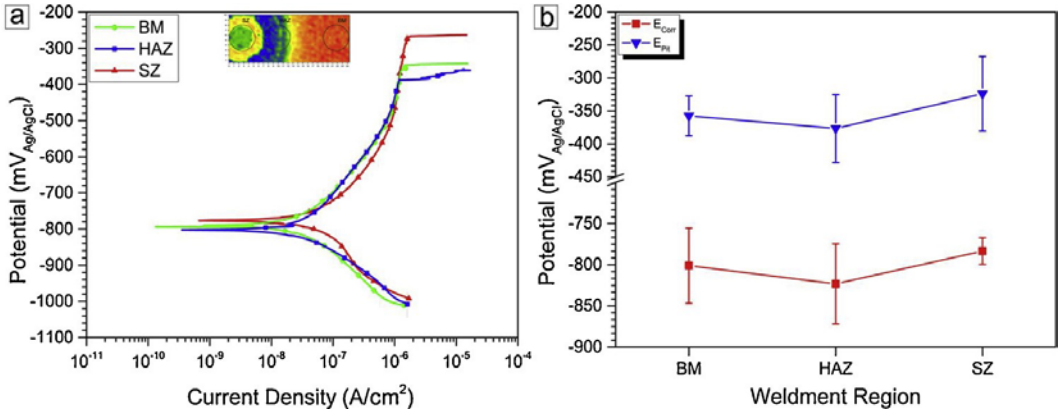

Fig. 8. (a) Polarization potenciodinamic tests obtained in 0.01 M NaCl and 0.1M Na_2SO_4 solutions from the distinct regions of a RFSS welded AA5754; (b) Corrosion potential (Ecorr) and pitting potential (Epit) results.

Aballe et al. [24], evaluating the influence of cathodic intermetallics on the reproducibility of the electrochemical measurements for an AA5083 alloy in NaCl solutions, observed that sample area reduction resulted in an increase of the dispersion in the values obtained for E_{corr}. The authors correlated this dispersion of values to the cathodic precipitate density present on the surface of the alloy during each new measurement, a fact which alters the sum and intensity between the rates of anodic and cathodic reactions. Similar results was reported by Vacchi et al. [11] who assessed the influence of RFSS welding on an AA6181-T4/Ti-6Al-4V welded joint and observed a high dispersion of results which occurred in both E_{corr} and E_{pit}. The study subsequently associated these results to the precipitate density variation. It should be included

that the dispersion reduction observed for E_{corr} in the SZ may be related to the superior homogenization of the precipitates in this region [Fig. 5(d) and (h)]. In addition, according to the mean results, the SZ is apparently the nobler region, i.e., it has the greatest values of E_{corr} and E_{pit} with respect to the HAZ and BM. These nobler values are consistent with the microstructure of the SZ region, which presented precipitates with a better distribution and smaller size due to the RFSS welding process promoting a break and homogenization of previous precipitates of the BM [11].

On the other hand, considering the small difference of E_{corr} and E_{pit} values between the samples, the polarization results are evidence that the RFSSW process has little to no significant negative influence on the localized corrosion behavior of the AA5754-H22 alloy.

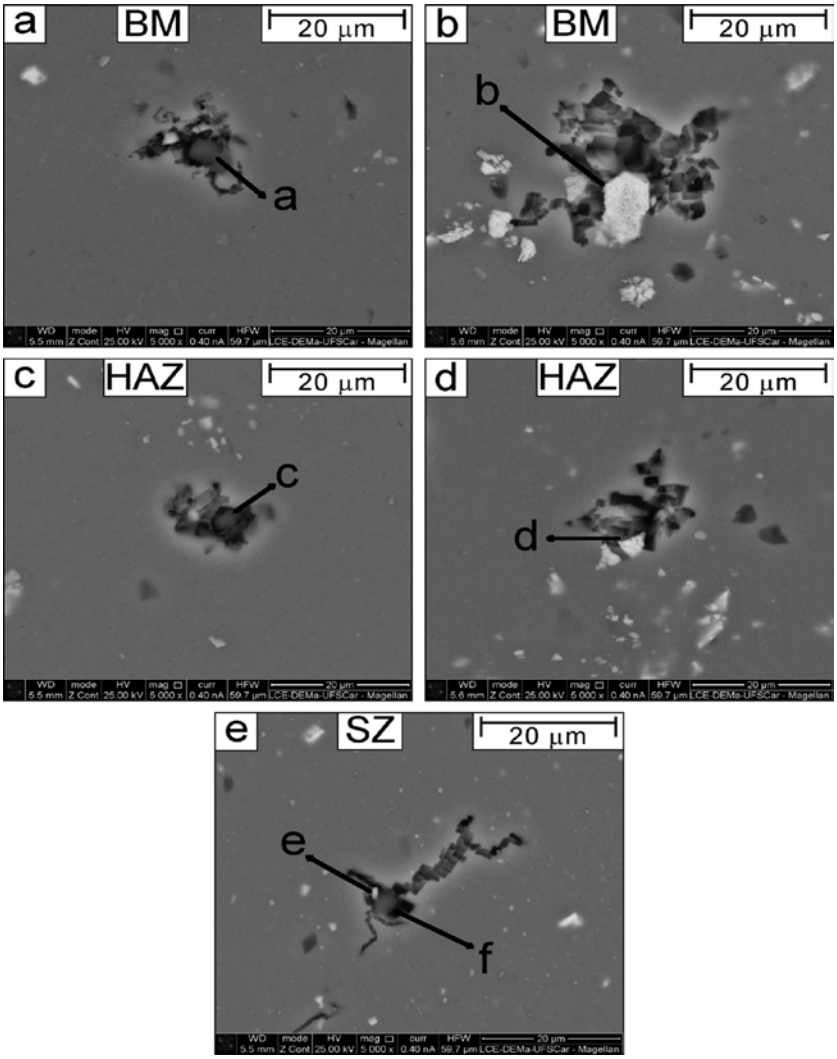

Fig. 9. Pit morphologies on the surface of the samples after potentiodynamic polarization in 0.01 M NaCl and 0.1 M Na_2SO_4 solutions: (a–b) BM, (c–d) HAZ and (e)

Fig. 9 shows the surface aspect of different welding regions after the potentiodynamic polarization tests, namely: the BM (a and b), HAZ (c and d) and SZ (e). Notice that in all regions, the pits nucleated adjacent to the Al (Fe, Si, Mn, Mg) and Mg_2Si precipitates (Table 3) and the corrosion attack intensity was higher in those regions with larger precipitates. The higher

corrosion attack intensity of the Al (Fe, Si, Mn, Mg) precipitates is caused by their cathodic behavior, with regards to the matrix that promoted the formation of a local galvanic cell between them. Hence, the precipitate size has a direct correlation to the intensity of formed galvanic cells and, thus, to the susceptibility of pitting corrosion, which is reduced when a “small cathode-large anode’’ mechanism is in operation. Similar results were observed within literature [11,25]. On the other hand, Mg_2Si precipitates initially present an anodic behavior in relation to the Al matrix, but as the corrosion process evolves, a silicon enrichment takes place inside the precipitates due to a preferential Mg dissolution, as can be observed when comparing the wt.% of Si before (Table 1) and after (Table 3) the potenciodinamic polarization tests. This silicon enrichment shifts the potential of the corroded Mg_2Si precipitates to a nobler direction, making them cathodic to the Al matrix. As a result, the Al matrix adjacent to the corroded Mg_2Si precipitates suffers anodic dissolution, thereby triggering pitting corrosion [26]. Consequently, if a “small cathode-large anode’’ mechanism is also in operation, the susceptibility to pitting corrosion is reduced.

Table 3 EDS composition analyses performed on precipitates near the pits.

Weld Region	Point	Composition (wt%)					
		Al	Mg	Si	Fe	Mn	O
BM	A	49.00	2.08	34.92	0.00	0.00	13.99
BM	B	73.56	1.80	0.35	20.34	1.59	0.00
HAZ	C	60.37	2.69	26.55	0.25	0.29	9.85
HAZ	D	81.94	2.75	0.20	13.05	1.10	0.96
SZ	E	75.90	2.69	11.04	4.97	1.70	3.70
SZ	F	62.45	2.61	22.80	0.00	0.00	12.15

Fig. 10 shows the representative Nyquist (a) and Bode (b) plots in a 0.5 M Na_2SO_4 solution at their respective E_{oc}. In Fig. 10(a), it can be seen that the three distintic RFSS welding regions (i.e., BM, HAZ and SZ) exhibit a capacitive time constant at high frequencies – which represents the charge-transfer reaction of a passivated AA5754-H22 surface. This behavior is followed by Warburg tail (straight line) at low frequencies, which is generally associated with oxygen diffusion [24,34], suggesting a similar corrosion mechanism between the distinct RFSS welding regions. However, the capacitive semicircle diameter of each region is remarkably different. This difference is directly associated with the distinct microstructures observed in the MO (Fig. 4) and SEM (Fig. 5) images that reflect in the charge transfer resistance at the metal/film interface and, consequently, to their different levels of corrosion resistance [27].

In addition, the larger capacitive semicircle is observed in the SZ, indicating that the protection afforded by the passive film formed in this region is better than that of the BM and HAZ regions. This result can be explained by the presence of a microstructure in this region that is more refined and homogeneous, which, in turn, provides an improved ability for forming a protective oxide film. Previous studies [28–30] have demonstrated an improvement in the electrochemical behavior of ultra-fine grained aluminum alloys when compared to their coarser-grain counterparts. The authors from the aforementioned literature related these results to (i) a decrease in intermetallic particle size, reducing the intensity of the galvanic cell formed between the aluminium matrix and precipitates, as well as (ii) the formation of a denser oxide film due to

the higher density of grain boundaries, facilitating the species diffusion and acting as nucleation (and pegging) sites of the passive film. Similar results were also reported by Qin et al. [31], who evaluated the corrosion behavior of the friction-stir-welded joints of a 2A14-T6 aluminum alloy. The authors reported that in comparison to the base material, the corrosion resistance of the welded regions is greatly improved as a result of the homogenization of the microstructure (promoted by the FSW process), which weakens the possibility of galvanic corrosion formation.

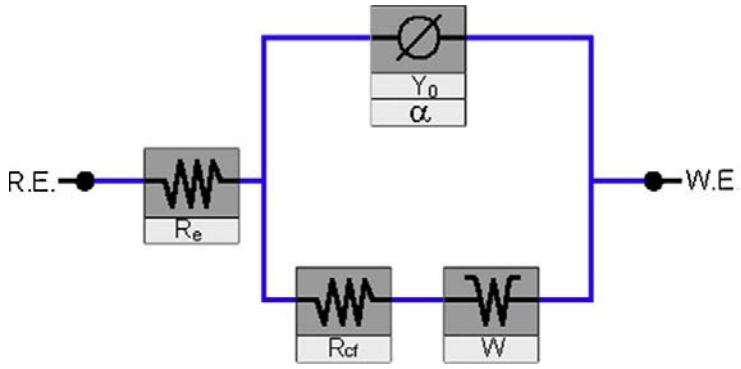

Fig. 10. EIS measurements of the distinct regions of a RFSS welded AA5754 in a 0.5 M Na_2SO_4 solution: (a) Nyquist plots (b) Bode plots.

Fig. 10(a) also illustrates that the diameter of capacitive semicircles suggests that the BM presents a better corrosion resistance than the HAZ. A possible hypothesis for this difference is the surface energy associated with these regions, due to the density and size of the precipitates being similar. It is well known that the cold working process improves the mechanical properties of a material by means of dislocation movements and dislocation generation within the crystal structure. This phenomenon also increases the surface energy of the material due to an increase in the density of surface crystalline defects (i.e., many of the dislocation lines intersect the surface of the material) [1]. Literature shows that the recovery process reduces surface energy by annihilating dislocations and the excess of energy is used in the recrystallization process, where new strain-free grains are formed [32]. Thus, a deformed microstructure (with higher surface energy), like the BM, will oxidize faster than a recrystallized microstructure, similar to HAZ, with lower surface energy, resulting in a thicker and more protective passive film [28–30].

In Fig. 10(b), the Bode plots of the samples display three distinct regions. The first region, which has high frequencies (between 3 kHz and 100 kHz), exhibits a IZI value of around 15 Ω cm^2 and phase angle values close to 0°, indicating that their impedance is dominated by the electrolyte resistance. In the second region, which has intermediate frequencies (between 0.3 Hz and 3 kHz), the Bode magnitude shows a linear slope that is close to -1 and the phase angles reach their maximum values (around -82°), which are characteristic responses of a capacitive behavior. The third region, which has low frequencies (between 0.01 Hz and 0.3 Hz), presents different IZI values for each welded region: 2.3×10^5 Ω *cm^2 for SZ, 1.5×10^5 Ω*cm^2 for BM and 1.1×10^5 Ω*cm^2 for HAZ. These results indicate that the corrosion resistance follows this order: SZ > BM > HAZ.

Additionally, it is observable that the change in phase angle values occurs in different frequencies for each welded region, around 1×10^{-2} Hz for the SZ, around 2.5×10^{-2} Hz for the BM and around 3×10^{-2} Hz for the HAZ, values that are related to the Warburg tail observed in the Nyquist Plot [Fig. 10(a)]. The phase angle change at higher frequencies in the HAZ region is directly linked to a lower charge transfer resistance in comparison to the BM and SZ. In this case, the reduction of dissolved oxygen ($2H_2O + O_2 + 4e^- \rightarrow 4OH^-$) occurs more rapidly in the HAZ region, resulting in an increase of OH- concentration in the cathodic regions of the Al surface. Meanwhile, in the anodic regions, the consumption of OH- results in the formation of a hydroxide ($Al^{3+} + 3OH \rightarrow Al(OH)_3$) [33,34].

Previous study [35] also shown that the presence of SO_4^{-2} anions in the solution promotes the formation of a basic salt due to a higher chemical affinity with the Al^{3+} cation in comparison to OH- anions, which could delay or avoid the formation of $Al(OH)_3$. This basic salt formed from the SO_4^{-2} anions can act similarly to the molybdate layer [36] that forms on the aluminum surface when this metal is in contact with solutions with high MoO_4^{-2} concentrations. According to Moshier et al. [37], this layer restricts the movement of oxygen and hydroxyl anions from penetrating the film and reaching the metal/film interface. Thus, the higher consumption of the reactive species (O_2-, OH-, SO_4^{-2}) at the metal/film interface in the HAZ due to their lower charge transfer resistance results in an increased deposition of the basic salt. In turn, this increased deposition hinders the mass transfer, causing the appearance of the Warburg impedance in higher frequencies when compared with the BM and the SZ.

In order to further analyze impedance and provide quantitative support for the experimental EIS data, a fitting procedure was carried out using the equivalent electric circuit (EEC), presented in Fig. 11. Similar EECs were used by several authors [27,33,38,39] for different materials, including aluminum, nickel and carbon steel alloys. Due to the fact that the surface of the AA5754-H22 alloy is in the passive state while in the SO_4^{-2} solution, the physical meaning of EEC elements can be described as follows: R_e represents the resistance of the electrolyte, R_{cf} is the polarization resistance associated with the charge transfer resistance of the passive oxide film, Ø (constant phase element – CPE) denotes the capacitive element associated with this oxide layer and W is a Warburg (diffusion) impedance element. The use of a CPE instead of an ideal capacitor was necessary due to frequency dispersion caused by inhomogeneities in the electrode surface (superficial roughness, impurities and porosity) and other sources of non-uniform current distribution. The impedance of a CPE (Z_{CPE}) is defined as:

$$Z_{CPE} = [Y_0 (j\omega)^{\alpha}]^{-1} \quad (1)$$

where Y_0 is a parameter related to the passive film capacitance (with dimensions of $S*s^{\alpha}/cm^2$); j is the imaginary number ($j^2 = -1$) ; ω is the angular frequency and α is an adjustable parameter, which represents the deviation from purely capacitive behavior, the value of which usually lies between -1 and 1. CPE describes an ideal capacitor for α = 1, a Warburg impedance with a diffusional character for α = 0.5, an ideal resistor for α = 0 and −1 for a pure inductor.

SZ.

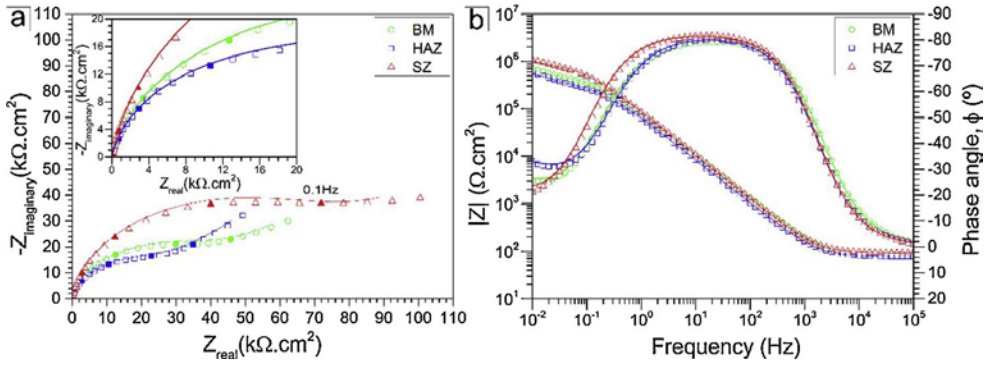

Fig. 11. Electrochemical equivalent circuit used for fitting EIS data measured at E_{oc}.

Table 4 displays the numerical values obtained (for all the parameters of the EEC) from the fitting of experimental EIS data. Note that the low χ^2 values (order of 10^{-4}) indicate a high quality fitting. In addition, the highest R_{cf} was obtained for the SZ (158.3 kΩ*cm²), followed by the BM (90.0 kΩ*cm²) and then the HAZ (63.9 kΩ*cm²), suggesting that the FSW process has an influence on the passive ability in the distinct welding regions of an AA5754-H22 alloy. This also aligns with the previous qualitative discussion about the EIS spectra and with the sequence of appearance of the Warburg's tail.

Table 4 Electrochemical parameters fitted from EIS data measured at individual E_{corr}.

Weld Region	R_e(Ω*cm²)	Y0(μS*s$^{\alpha}$ /cm²)	α	R_{cf}(kΩ*cm²)	W(μS*s$^{1/2}$/cm²)	χ^2 (x 10^{-4})
BM	17.1 ± 0.3	12.0 ± 1.7	0.90 ± 0.01	90.0 ± 14.3	57.4 ± 5.1	4.64 ± 3.8
HAZ	16.6 ± 0.2	13.1 ± 0.9	0.90 ± 0.01	63.9 ± 5.9	48.6 ± 3.8	3.48 ± 0.7
SZ	19.2 ± 0.3	9.8 ± 0.3	0.91 ± 0.01	158.3 ± 7.6	50.1 ± 11.2	6.63 ± 4.4

As the obtained values for α parameter (~ 0,90) in the three distintic RFSS welding regions approach that of an ideal capacitor (α = 1), their respective capacitance can be calculated by the equation of Brug [40]:

$$C = Y0^{1/\alpha} (R_e^{-1} + R_{cf}^{-1})^{(\alpha - 1)/\alpha} \quad (2)$$

It is well established that the capacitance response of a layer is an indication of their thickness, due to the fact that they are inversely proportional quantities. So, after calculating the capacitance of the passive film formed on the distintic RFSS welding regions, estimating their respective film thickness was possible on the basis of Eq. 3, which is valid for the parallel plate capacitor model of a homogenous oxide layer [41].

$$d = \frac{\varepsilon_0 \varepsilon_r}{C} \quad (3)$$

Where d is the thickness of barrier layer, ε_r is the dielectric constant of the passive film, ε_0 is the vacuum permittivity (8.854 × 10^{-14} F cm^{-1}) and C is the capacitance (in F/cm²). It is difficult to obtain an accurate thickness value for the passive film because the dielectric constant (ε_r) is not well established. Martin et al [42], who studies the impedance of the passive film on aluminum, used a relative dielectric constant (ε_r) value of 40, thus, this value was considered in the present study.

Table 5 Passive film thicknesses obtained through EIS measurements.

Weld Region	Capacitance ($\mu F/cm^2$)	Thickness (nm)
BM	4.67	7.48
HAZ	5.13	6.90
SZ	4.17	8.49

Table 5 presents the capacitance and passive film thickness of each welded region. Note that the thickness value of the passive film increased in the following order: HAZ (6.90 nm) < BM (7.58 nm) < SZ (8.49 nm). These results indicate that the SZ has a thicker passive film than other welded regions and corroborates with the polarization and EIS results, where it can be seen that a more refined microstructure presents a better corrosion resistance. The results of the current study also agree substantially with previous literature, which report that the passive film of aluminum in different media is around 2−10 nm
[43–45].

4. **Conclusions**

The microstructure evolution and electrochemical corrosion behavior of the refill friction stir spot welding process on the surface of the AA575-H22 alloy were investigated. Based on the experimental results, the following conclusion can be drawn:

- The thermomechanical cycle imposed by the RFSSW process promotes microstructural changes, making the SZ microstructure more homogeneous and refined;
- RFSSW process promotes different hardness values along the welded joint, with a higher hardness observed in the BM and a lower hardness in the HAZ region;
- The refined microstructure of SZ presents the higher localized corrosion resistance. In addition, the pits nucleate preferentially in areas adjacent to the Al (Fe, Si, Mn, Mg) and Mg_2Si precipitates in all studied regions;
- Due to the more homogeneous and better refined microstructure in the SZ region, the passive film formed on this region is thicker and more protective than that on the BM and HAZ;
- The achieved results are evidence that the RFSSW process is an interesting alternative for the welding of overlapping dissimilar joints.

Acknowledgements

The authors gratefully acknowledge CAPES (Coordination for the Improvement of Higher Education Personnel) and PPGCEM/UFSCar (Materials Science and Engineering Postgraduate Program at the Federal University of São Carlos). Additionally, the authors would like to thank the Brazilian research funding agency, CNPq (National Council for Scientific and Technological

Development – grant no.311163/20173), for their financial support of this study and the Helmholtz Association of German Research Centres for their technical support.

References

[1] G.E. Totten, D.S. MacKenzie, Handbook of aluminum, 1st ed., Physical Metallurgy and Processes Vol. 1 Marcel Dekker, Inc, New York, 2003, https://doi.org/10.1201/9780203912607.

[2] F. Möller, C. Thomy, F. Vollertsen, Joining of titanium-aluminium seat tracks for aircraft applications – properties, Weld. World. 56 (2012) 108–114, https://doi.org/10.1007/BF03321341.

[3] F. Möller, M. Grden, C. Thomy, F. Vollertsen, Combined laser beam welding and brazing process for aluminium titanium hybrid structures, Phys. Procedia 12 (2011) 215–223, https://doi.org/10.1016/j.phpro.2011.03.028.

[4] M.K. Kulekci, U. Esme, O. Er, Experimental comparison of resistance spot welding and friction-stir spot welding processes for the en aw 5005 aluminum alloy, Mater. Tehnol. 45 (2011) 395–399.

[5] G.M. Ji, X.G. Cai, L. Zhang, H. Lai, B.W. Zhao, Comparison research of aircraft panels connected by friction stir welding and riveting, Appl. Mech. Mater. 668–669 (2014) 3–7, https://doi.org/10.4028/www.scientific.net/AMM.668-669.3.

[6] R.S. Mishra, Z.Y. Ma, Friction stir welding and processing, Mater. Sci. Eng. R Rep. 50 (2005) 1–78, https://doi.org/10.1016/j.mser.2005.07.001.

[7] S. Emami, T. Saeid, R.A. Khosroshahi, Microstructural evolution of friction stir welded SAF 2205 duplex stainless steel, J. Alloys Compd. 739 (2018) 678–689, https://doi.org/10.1016/j.jallcom.2017.12.310.

[8] C. Zhang, L. Cui, Y. Liu, C. Liu, H. Li, Microstructures and mechanical properties of friction stir welds on 9 % Cr reduced activation ferritic/martensitic steel, J. Mater. Sci. Technol. 34 (2018) 756–766, https://doi.org/10.1016/j.jmst.2017.11.049.

[9] Y. Li, C. Liu, L. Yu, H. Li, Z. Wang, Y. Liu, W. Li, Effect of high-temperature ageing on microstructure and mechanical properties of linear friction welded S31042 steel joint, Acta Metall. Sin. 54 (2018) 981–990, https://doi.org/10.11900/0412.1961. 2017.00483.

[10] U. Suhuddin, L. Campanelli, M. Bissolatti, H. Wang, R. Verastegui, J.F. dos Santos, A review on microstructural and mechanical properties of friction spot welds in Albased similar and dissimilar joints, in: H. Fujii (Ed.), Proc. 1st Int. Jt. Symp. Join. Weld. Woodhead Publishing, 2013, pp. 15–21, , https://doi.org/10.1533/978-178242-164-1.15.

[11] G.S. Vacchi, A.H. Plaine, R. Silva, V.L. Sordi, U.F.H. Suhuddin, N.G. Alcântara, S.E. Kuri, C.A.D. Rovere, Effect of friction spot welding (FSpW) on the surface corrosion behavior of overlapping AA6181-T4/Ti-6Al-4V joints, Mater. Des. 131 (2017) 127–134, https://doi.org/10.1016/j.matdes.2017.06.005.

[12] A. O'Brien, Welding Handbook, 9th ed., AWS, Miami, 2007.

[13] A.H. Plaine, U.F.H. Suhuddin, C.R.M. Afonso, N.G. Alcântara, J.F. dos Santos, Interface formation and properties of friction spot welded joints of AA5754 and Ti6Al4V alloys, Mater. Des. 93 (2016) 224–231, https://doi.org/10.1016/j.matdes. 2015.12.170.

[14] A.H. Plaine, A.R. Gonzalez, U.F.H. Suhuddin, J.F. dos Santos, N.G. Alcântara, A.H. Plaine, A.R. Gonzalez, U.F.H. Suhuddin, J.F. dos Santos, N.G. Alcântara, Process parameter optimization in friction spot welding of AA5754 and Ti6Al4V dissimilar joints

using response surface methodology, Int. J. Adv. Manuf. Technol. 83 (2015) 36–41, https://doi.org/10.1007/s00170-015-8055-5.

[15] A.H. Plaine, U.F.H. Suhuddin, N.G. Alcântara, J.F. dos Santos, Fatigue behavior of friction spot welds in lap shear specimens of AA5754 and Ti6Al4V alloys, Int. J. Fatigue 91 (2016) 149–157, https://doi.org/10.1016/j.ijfatigue.2016.06.005.

[16] W.-J. Lee, S.-I. Pyun, Effects of sulphate ion additives on the pitting corrosion of pure aluminium in 0.01 M NaCl solution, Electrochim. Acta 45 (2000) 1901–1910, https://doi.org/10.1016/S0013-4686(99)00418-1.

[17] M. Peel, A. Steuwer, M. Preuss, P.J. Withers, Microstructure, mechanical properties and residual stresses as a function of welding speed in aluminium AA5083 friction stir welds, Acta Mater. 51 (2003) 4791–4801, https://doi.org/10.1016/S13596454(03)00319-7.

[18] R.W. Fonda, P.S. Pao, H.N. Jones, C.R. Feng, B.J. Connolly, A.J. Davenport, Microstructure, mechanical properties, and corrosion of friction stir welded Al 5456, Mater. Sci. Eng. A 519 (2009) 1–8, https://doi.org/10.1016/j.msea.2009.04. 034.

[19] C.B. Fuller, M.W. Mahoney, The effect of friction stir processing on 5083-H321/
5356 Al arc welds: microstructural and mechanical analysis, Metall. Mater. Trans. A 37 (2006) 3605–3615, https://doi.org/10.1007/s11661-006-1055-1.

[20] R. Ambat, A.J. Davenport, G.M. Scamans, A. Afseth, Effect of iron-containing intermetallic particles on the corrosion behaviour of aluminium, Corros. Sci. 48 (2006) 3455–3471, https://doi.org/10.1016/j.corsci.2006.01.005.

[21] M.M. Attallah, C.L. Davis, M. Strangwood, C.L. Davis, M. Strangwood, Influence of base metal microstructure on microstructural development in aluminium based alloy friction stir welds, Sci. Technol. Weld. Join. 12 (2007) 361–369, https://doi. org/10.1179/174329307X164238.

[22] T.R. McNelley, S. Swaminathan, J.Q. Su, Recrystallization mechanisms during friction stir welding/processing of aluminum alloys, Scr. Mater. 58 (2008) 349–354, https://doi.org/10.1016/j.scriptamat.2007.09.064.

[23] R. Reed-Hill, R. Abbaschian, R. Abbaschia, Physical Metallurgy Principles, Cengage Learning, Stamford, 2010.

[24] A. Aballe, M. Bethencourt, F.J. Botana, M.J. Cano, M. Marcos, Influence of the cathodic intermetallics distribution on the reproducibility of the electrochemical measurements on AA5083 alloy in NaCl solutions, Corros. Sci. 45 (2003) 161–180, https://doi.org/10.1016/S0010-938X(02)00067-7.

[25] J.H. Jiang, A.B. Ma, F.M. Lu, N. Saito, A. Watazu, D. Song, P. Zhang, Y. Nishida, Improving corrosion resistance of Al-11mass%Si alloy through a large number of ECAP passes, Mater. Corros. 62 (2011) 848–852, https://doi.org/10.1002/maco. 200905521.

[26] F.L. ZENG, Z.L. Wei, J.F. Li, C.X. Li, X. TAN, Z. ZHANG, Z.Q. ZHENG, Corrosion mechanism associated with Mg2Si and Si particles in Al-Mg-Si alloys, Trans. Nonferrous Met. Soc. China (English Ed.) 21 (2011) 2559–2567, https://doi.org/10.1016/S1003-6326(11)61092-3.

[27] Y. Liu, G.Z. Meng, Y.F. Cheng, Electronic structure and pitting behavior of 3003 aluminum alloy passivated under various conditions, Electrochim. Acta 54 (2009) 4155–4163, https://doi.org/10.1016/j.electacta.2009.02.058.

[28] K.D. Ralston, D. Fabijanic, N. Birbilis, Effect of grain size on corrosion of high purity aluminium, Electrochim. Acta 56 (2011) 1729–1736, https://doi.org/10.1016/j. electacta.2010.09.023.

[29] M.K. Chung, Y.S. Choi, J.G. Kim, Y.M. Kim, J.C. Lee, Effect of the number of ECAP pass time on the electrochemical properties of 1050 Al alloys, Mater. Sci. Eng. A. 366 (2004) 282–291, https://doi.org/10.1016/j.msea.2003.08.056.

[30] D. SONG, Ab. MA, Jh. JIANG, Ph. LIN, Dh. YANG, Corrosion behavior of ultra-fine grained industrial pure Al fabricated by ECAP, Trans. Nonferrous Met. Soc. China (English Ed. 19 (2009) 1065–1070, https://doi.org/10.1016/S1003-6326(08) 60407-0.

[31] H. long Qin, H. Zhang, D. tong Sun, Q. yu Zhuang, Corrosion behavior of the friction-stir-welded joints of 2A14-T6 aluminum alloy, Int. J. Miner. Metall. Mater. 22 (2015) 627–638, https://doi.org/10.1007/s12613-015-1116-9.

[32] J.E. Hatch, Aluminum Properties and Physical Metallurgy, ASM, Ohio, US, 1984, p. 424, https://doi.org/10.1361/appm1984p001.

[33] W. Xu, J. Liu, Microstructure and pitting corrosion of friction stir welded joints in 2219-O aluminum alloy thick plate, Corros. Sci. 51 (2009) 2743–2751, https://doi.org/10.1016/j.corsci.2009.07.004.

[34] J.H.W. de Wit, H.J.W. Lenderink, Electrochemical impedance spectroscopy as a tool to obtain mechanistic information on the passive behaviour of aluminium, Electrochim. Acta 41 (1996) 1111–1119, https://doi.org/10.1016/0013-4686(95) 00462-9.

[35] J.B. Bessone, D.R. Salinas, C.E. Mayer, M. Ebert, W.J. Lorenz, An EIS study of aluminium barrier-type oxide films formed in different media, Electrochim. Acta 37 (1992) 2283–2290, https://doi.org/10.1016/0013-4686(92)85124-4.

[36] K.-H. Na, S.-I. Pyun, Effect of sulphate and molybdate ions on pitting corrosion of aluminium by using electrochemical noise analysis, J. Electroanal. Chem. Lausanne (Lausanne) 596 (2006) 7–12, https://doi.org/10.1016/j.jelechem.2006.06.017.

[37] W.C. Moshier, G.D. Davis, Interaction of molybdate anions with the passive film on aluminum, Corrosion 46 (1990) 43–50, https://doi.org/10.5006/1.3585065.

[38] Z.F. Yin, W.Z. Zhao, W.Y. Lai, X.H. Zhao, Electrochemical behaviour of Ni-base alloys exposed under oil/gas field environments, Corros. Sci. 51 (2009) 1702–1706, https://doi.org/10.1016/j.corsci.2009.04.019.

[39] J. Tang, Y. Shao, J. Guo, T. Zhang, G. Meng, F. Wang, The effect of H2S concentration on the corrosion behavior of carbon steel at 90 °C, Corros. Sci. 52 (2010) 2050–2058, https://doi.org/10.1016/j.corsci.2010.02.004.

[40] G.J. Brug, A.L.G. van den Eeden, M. Sluyters-Rehbach, J.H. Sluyters, The analysis of electrode impedances complicated by the presence of a constant phase element, J. Electroanal. Chem. Interfacial Electrochem. 176 (1984) 275–295, https://doi.org/10.1016/S0022-0728(84)80324-1.

[41] C.A. Della Rovere, J.H. Alano, R. Silva, P.A.P. Nascente, J. Otubo, S.E. Kuri, Characterization of passive films in shape stainless steel steels, Corros. Sci. 57 (2012) 154–161, https://doi.org/10.1016/j.corsci.2011.12.022.

[42] F.J. Martin, G.T. Cheek, W.E. O'Grady, P.M. Natishan, W.E. O'Grady, P.M. Natishan, Impedance studies of the passive film on aluminium, Corros. Sci. 47 (2005) 3187–3201, https://doi.org/10.1016/j.corsci.2005.05.058.

[43] J.B. Bessone, D.R. Salinas, C.E. Mayer, M. Ebert, W.J. Lorenz, An EIS study of aluminium barrier-type oxide films formed in different media, Electrochim. Acta 37 (1992) 2283–2290, https://doi.org/10.1016/0013-4686(92)85124-4.

[44] G.S. Frankel, Pitting corrosion of metals, J. Electrochem. Soc. 145 (1998) 2186, https://doi.org/10.1149/1.1838615.

[45] R.W. Revie, H.H. Uhlig, Corrosion and Corrosion Control, 4th ed., John Wiley & Sons, Inc., Hoboken, NJ, USA, 2008, https://doi.org/10.1002/9780470277270.